Official journal of the CIOMP 2047-7538
www.nature.com/lsa

ARTICLE Open Access

Anisotropic phonon dynamics in Dirac semimetal $PtTe_2$ thin films enabled by helicity-dependent ultrafast light excitation

Ziyang Li[1], Yequan Chen[2], Anke Song[2], Jinzhong Zhang[3], Rong Zhang[2,4], Zongzhi Zhang[1]✉ and Xuefeng Wang[2]✉

Abstract

Coherent phonons have aroused considerable attention in condensed matter physics owing to their extraordinary capacity of reflecting and controlling the physical properties of matter. However, the investigation on the interaction between coherent phonons and other microscopic particles on the ultrafast timescale within topological systems continues to be an active and unresolved area. Here, we show the energy transfer of coherent optical phonons (COP) in Dirac semimetal $PtTe_2$ thin films using ultrafast optical pump-probe spectroscopy. Specifically, the helicity-dependent light-driven anisotropic COP signals disclose their direct connection with the light-excited anisotropic spin-polarized electrons via an angular momentum transfer. Furthermore, we observe the notable decreases in the COP oscillation frequency and the decay rate with increasing temperatures due to the anharmonic phonon-phonon scattering and electron-phonon scattering in the COP dissipation process, respectively. Our work paves the way for uncovering the coherent phonons in Dirac semimetals for the potential applications in optoelectronics and opto-spintronics.

Introduction

In condensed matter physics, topological Dirac semimetals[1–4] have attracted great interest due to their unique electronic band structures, which provide an ideal platform to investigate topological phase transition and the low-energy excitation of elementary particles[5,6]. $PtTe_2$, a 2D layered van der Waals material in the transition metal dichalcogenide (TMD) family, possesses type-II Dirac fermions with a pair of strongly tilted and anisotropic Dirac cones[7]. The de Haas-van Alphen quantum oscillations further disclose an anisotropic Dirac band structure, which is accompanied with the low effective mass and the high carrier mobility[8,9]. In view of the high charge-to-spin conversion efficiency[10], superior high conductivity[11,12], excellent air stability[13], dimensionality-mediated semimetal-semiconductor transition[14–16], and broadband photoresponse from visible to terahertz range[15,17], $PtTe_2$ has become a promising candidate for spintronic[10] and optoelectronic devices[15,17–20]. Very recently, the helicity-dependent terahertz emission has been observed in the inversion-symmetry-broken $PtTe_2$ thin films[21], further expanding the potential application range.

Coherent phonons represent the collective lattice vibrations that are in-phase, classified as coherent optical phonons (COP) and coherent acoustic phonons (CAP), which are recognized as effective tools for controlling fundamental physical properties and exploring the ultrafast dynamic processes of spins and carriers[22,23]. For example, through coherent phonons researchers have demonstrated the manipulation of macroscopic magnetic states in orthoferrite[24], the ultrafast phase transitions from insulator to metal states[25], and the enhancement of superconductivity[26]. Ultrafast optical pump-probe

Correspondence: Zongzhi Zhang (zzzhang@fudan.edu.cn) or Xuefeng Wang (xfwang@nju.edu.cn)
[1]Key Laboratory of Micro and Nano Photonic Structures (MOE), School of Information Science and Technology, Fudan University, Shanghai, China
[2]Jiangsu Provincial Key Laboratory of Advanced Photonic and Electronic Materials, State Key Laboratory of Spintronics Devices and Technologies, School of Electronic Science and Engineering, Collaborative Innovation Center of Advanced Microstructures, Nanjing University, Nanjing, China
Full list of author information is available at the end of the article
These authors contributed equally: Ziyang Li, Yequan Chen

spectroscopy is a powerful tool for revealing the quasiparticle dynamics in the time domain. Through the time-resolved stimulated Raman scattering with picosecond laser pulses, Alfano and Shapiro firstly achieved the direct measurement of the COP lifetime in a calcite crystal[27]. Following this, they further observed the decay route of the methyl vibrations in ethanol[28]. Later, the exploration of lattice vibrations was expanded to a variety of conventional liquid and solid materials[29,30]. In recent years, the advancements of ultrafast laser techniques have facilitated the exploration of more COP-mediated interactions, enabling deeper understanding of complex physical phenomena in various quantum materials, such as topological insulators[22], Weyl semimetals[23], and Dirac semimetals[31]. For the Dirac semimetal $PtTe_2$, most phonon studies only utilized the frequency-domain spontaneous Raman scattering[10,12,21]. Temporal behaviors of phonons, however, have rarely been reported in time-resolved measurements[32]. Therefore, it is urgent to explore the systematic temporal behaviors of coherent phonons to regulate the topological properties as well as optimize the performance of $PtTe_2$-based optoelectronic devices.

In this work, the dynamics of coherent phonons in $PtTe_2$ thin films is explored at various temperatures by ultrafast optical pump-probe technique. During the photoexcitation process, coherent phonons excited by the pump beam periodically modulate the local dielectric constant, which is monitored by the transient changes of the polarization of the probe beam. We detect the COP of the E_g vibrational mode and the longitudinal CAP excited by circularly polarized (CP) light. Interestingly, the COP exhibit helicity-dependent amplitudes and phases, as well as obvious anisotropy with respect to the polarization direction of the probe beam. Such an anisotropic behavior is ascribed to the coupling between laser-excited spin-polarized electrons and COP. Temperature-dependent measurements of lattice dynamics further show a clear redshift of the E_g-phonon frequency and an unusual decrease in the vibrational decay rate with increasing temperatures. These findings benefit a deep understanding of phonon dynamics for a myriad of quantum materials.

Results

The basic structural properties of $PtTe_2$ films

The high-quality $PtTe_2$ thin films with a thickness of ~20 nm were grown on the sapphire substrates by pulsed laser deposition (PLD). Details of the sample growth process can be seen in "Materials and methods" section. The $PtTe_2$ films possess a trigonal CdI_2-type crystal structure with space group $P\bar{3}m1$ (NO. 164). It has a layered structure with the adjacent Te layers held together by van der Waals interaction in different monolayers and the Pt layer sandwiched between two Te layers in each monolayer, as schematically shown in the side and top views of Fig. 1a, b. Each Pt atom is surrounded by six Te atoms in a hexagonal periodic structure. Figure 1c displays a series of (00n) X-ray diffraction (XRD) peaks related to $PtTe_2$ and sapphire, suggesting that these films are epitaxially grown along the [001] direction of the substrates. The Raman spectrum in Fig. 1d shows the characteristic peaks of E_g (~3.33 THz, 111 cm^{-1}) and A_{1g} (~4.71 THz, 157 cm^{-1}) vibration modes for 1T-$PtTe_2$[33]. The E_g mode corresponds to in-plane relative motion of the bottom and top Te atoms in opposite directions, while A_{1g} is the out-of-plane vibration mode of the Te atoms.

Ultrafast dynamics of $PtTe_2$ films

The femtosecond laser pump-probe setups, with either elliptically polarized or linearly polarized pump beam excitation, are schematically displayed in Fig. 1e, f, respectively. An intense femtosecond pump beam is used to excite the lattice dynamics of $PtTe_2$, which can be detected by the reflected probe beam passing through a balanced photodetector. The variation of polarization direction is acquired from the differential signals ($\Delta I = I_S - I_P$), which simultaneously reflect the transient changes of magneto-optical Kerr effect and anisotropic reflectivity (see "Materials and methods" section for details).

As shown in Fig. 1e, we use the all-optical time-resolved pump-probe technique to measure the ultrafast dynamics of the $PtTe_2$ films upon the right-handed ($+\sigma$, $\phi_{\lambda/4} = 45°$) and left-handed ($-\sigma$, $\phi_{\lambda/4} = 135°$) CP light excitation. The linearly-polarized (LP) probe beam is along the P-polarization (P-pol) direction. The ellipticity angle $\phi_{\lambda/4}$ of the pump beam is defined as the angle between P-pol and fast axis of a quarter-wave plate (QWP). Figure 2a shows the typical time-domain traces of the differential signals ΔI in the delay time range of 0–6 ps. In transient reflectivity or transmission spectroscopy, light excitation generally leads to an immediate rise/fall at nearly zero delay time due to photo-bleaching/photo-absorption, with the response time limited by the pulse duration of the femtosecond laser. However, an abrupt bipolar peak is observed when the delay time is within 1 ps with an inverted shape upon $\pm\sigma$ light excitation, which is attributed to optically spin-injection-induced Kerr rotation because the photoexcited hot electrons are transiently spin-polarized upon absorbing the angular momentum ($\pm\hbar$) of $\pm\sigma$ photons[34]. From the subsequent spin relaxation process, we observe the spin depolarization within 1 ps and an attached high-frequency oscillation. Figure 2b exhibits the corresponding fast Fourier transform (FFT) frequency spectra, where a distinct terahertz mode with the central frequency ~3.2 THz can be recognized. The vibrational energy of ~13.23 meV matches E_g mode phonon in Raman spectrum, therefore, the oscillation

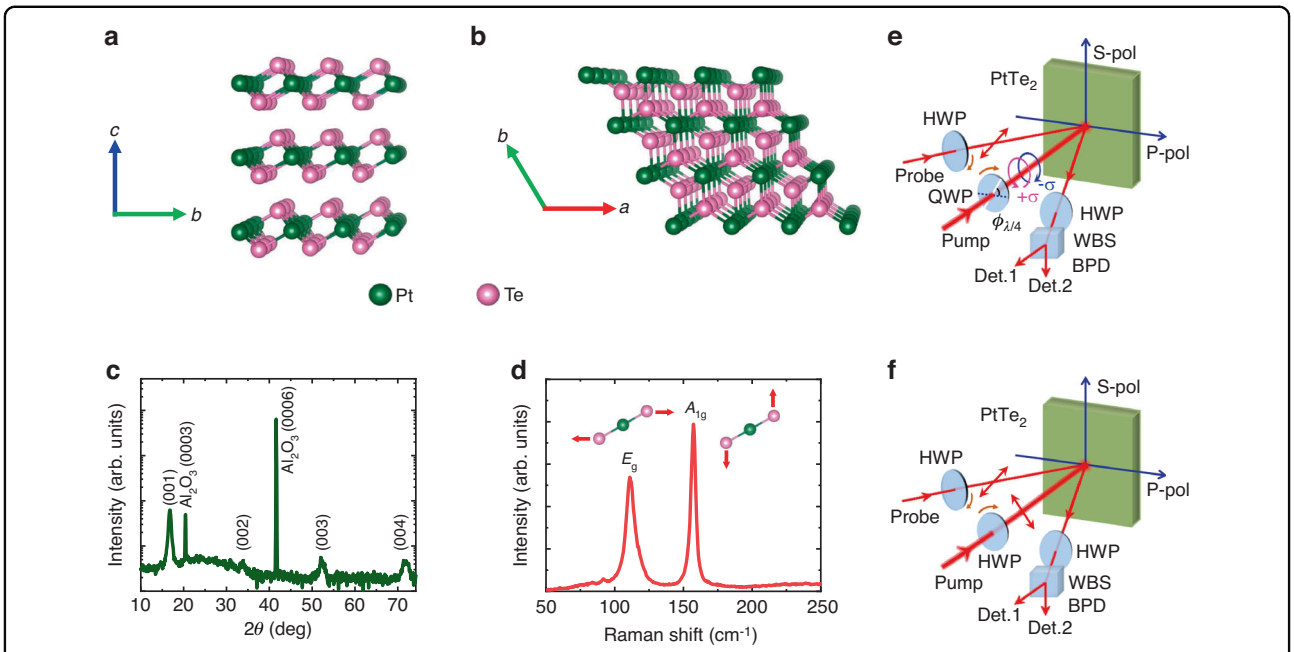

Fig. 1 Crystal structure of $PtTe_2$ and the optical pump-probe setup. a, **b** The side and top views of the $PtTe_2$ crystal structure, respectively. Green and pink spheres represent the Pt and Te atoms, respectively. **c**, **d** The XRD pattern and Raman spectrum of $PtTe_2$ films, respectively. **e**, **f** The schematic diagrams of the femtosecond laser pump-probe setup with elliptically polarized and linearly polarized pump beam excitation, respectively. The ellipticity angle $\phi_{\lambda/4}$ denotes the angle between P-polarization (P-pol) and fast axis of a quarter-wave plate. QWP quarter-wave plate. HWP half-wave plate. WBS Wollaston beam splitter. Det. 1 and Det. 2 a pair of channels of balanced photodetector (BPD). S-pol S-polarization

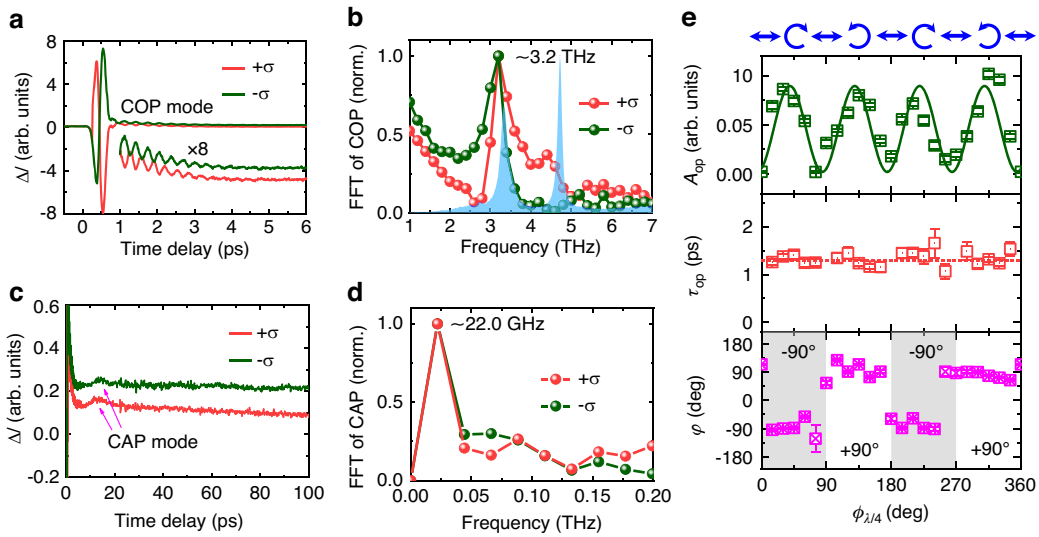

Fig. 2 All-optical generation and detection of coherent phonons and helicity-dependent COP. a The photoinduced time-domain differential signals (ΔI) as a function of delay time. **b** The corresponding FFT spectra derived from (**a**). The blue shadow area in (**b**) shows the result from the Raman spectrum. **c**, **d** The transient signals for the longer time delay range and the corresponding FFT spectra. **e** The fitted parameters of A_{op}, τ_{op}, and φ versus $\phi_{\lambda/4}$. The solid green line is fitted with a sine function

mode is considered as the in-plane COP of E_g mode. Nevertheless, the component from out-of-plane COP of A_{1g} mode is negligible although the intensity of the A_{1g} mode is slightly greater than that of the E_g mode in Raman spectrum (Fig. 1d). Notably, the COP vibration undergoes a 180° phase shift as the pump light changes from $+\sigma$ to $-\sigma$, which is closely linked to the spin-polarized electrons within the delay time of 1 ps.

Figure 2c shows the transient ΔI signal within a longer delay time range of 100 ps. A pair of valley and peak (marked with the purple arrows) can be identified during 6–13 ps, which corresponds to the lattice vibration of low-frequency longitudinal CAP with ~22 GHz (Fig. 2d). The oscillation of CAP signals exhibits only one full cycle, which is ascribed to the fact that the laser penetration length is comparable to the thickness of the sample (see Supplementary Note 1). Different from the opposite vibrational phase of COP, the CAP vibration remains in phase for the pump light with $\pm\sigma$ helicity, which is consistent with the origin of the laser heating effect. After subtracting the CAP and COP oscillation signals, the background dynamic process with time delay longer than 1 ps is well-fitted by a biexponential decay function, turning out two carrier lifetimes of $\tau_1 \approx 1$ ps and $\tau_2 > 100$ ps. The transient τ_1 is due to the hot-carrier cooling by electron-phonon scattering and the long-lived τ_2 denotes the phonon-assisted electron-hole recombination[23].

Helicity-dependent phonons in $PtTe_2$ films

To definitively determine the relation between optically spin injection and the COP feature, the time-domain traces are measured for pump pulses with variable elliptical polarization by rotating a QWP (Fig. 1e), namely changing angle $\phi_{\lambda/4}$ and fixing the LP probe beam at P-pol direction. The curves are fitted by the following equation[35]:

$$\begin{aligned}\Delta I(t) = D_0 + A_{\mathrm{e-ph}} \exp\left(-\tfrac{t-t_0}{\tau_{\mathrm{e-ph}}}\right) \\ + A_{\mathrm{op}} \exp\left(-\tfrac{t-t_0}{\tau_{\mathrm{op}}}\right) \sin[2\pi f(t-t_0)+\varphi]\end{aligned} \quad (1)$$

where D_0 is a fitting constant related to the background signal, the second term represents the non-oscillatory signal resulting from the relaxation process of photo-excited hot carriers via electron-phonon scattering, which is independent of $\phi_{\lambda/4}$, and the last term is the oscillatory COP component. A_{op}, τ_{op}, f, and φ in the last term are the vibration amplitude, lifetime, frequency, and initial phase, respectively. The fitted constant value of $\tau_{\mathrm{e\text{-}ph}}$ is about 1.2 ps, in good agreement with the reported electron-acoustic phonon scattering time[22]. The fitted f of COP is ~3.17 THz, coincident with the FFT result (Fig. 2b). Figure 2e shows the fitted τ_{op}, A_{op}, and φ as a function of $\phi_{\lambda/4}$. Specifically, the value of τ_{op} keeps almost unchanged (~1.3 ps), indicating that the interaction of photon, electron, and phonon just modulates the generation of COP at the very beginning upon laser excitation. While the following relaxation process of COP is mainly influenced by the intrinsic phonon-phonon and electron-phonon scattering of $PtTe_2$, as discussed below. The helicity-dependent A_{op} shows a definite sine-function fitting, indicating only the helical light can excite the visible lattice vibration. The COP phase strictly relies on the laser helicity. As such, the pump light with opposite helicity drives the lattice motion in the opposite direction, indicating the connection between optically spin injection and the lattice dynamics of the COP component.

In general, there are two mechanisms responsible for the production of COP by ultrafast laser pulses, namely the impulsive stimulated Raman scattering (ISRS) in transparent materials[36] and the displacive excitation of coherent phonon (DECP) in opaque materials[37]. ISRS enables the excitation of all Raman-active phonon modes with different symmetries, whereas DECP is limited to the fully symmetric modes that are displaced without varying the crystal symmetry. By examining the ultrafast absorption spectra[32], a fully symmetric A_{1g} mode COP with a vibration frequency of ~4.68 THz is observed in the $PtTe_2$ films due to the DECP mechanism. In other TMD materials such as WSe_2[38], $TiTe_2$[39], and $NiTe_2$[31], the displacive A_{1g}-COP have been also detected by the optical pump-probe technique. Notably, the E_g-COP are also observable in our $PtTe_2$ films, which is usually absent in other TMD materials. Considering that the displacement of E_g vibration lowers the crystal symmetry, the E_g-COP in the literature is commonly ascribed to the ISRS excitation[40].

The COP excitation by ISRS should obey the theory of transient stimulated Raman scattering (TSRS). In the TSRS model, the amplitude of coherent atomic motion is associated with the Raman tensor and the electric field directions of the LP pump and probe light[41]. However, the amplitude of purely displacive COP should be proportional to the density of photoexcitation electrons dependent on the optical absorption. To clarify this phenomenon, the time-resolved curves were measured after LP pump beam excitation. The polarization angle (α) of the incident probe beam varies from 0° to 180° by rotating a half-wave plate (HWP), while the LP pump beam is fixed along the P-pol direction ($\beta = 0°$) (Fig. 1f). The phonon vibrations become notably stronger when α approaches 45° and 135°, as shown in Fig. S1, and it is observed that the vibration phase is opposite between the two angular ranges of $\alpha = 0$–90° and 90–180°. Figure 3a summarizes the values of A_{op} of E_g-COP as a function of α, derived from the FFT spectra. Figure 3b shows the β-dependent A_{op}, in which the polarization angle of the LP pump beam is varied ($\beta = 0$–180°) with the unchanged P-pol probe beam ($\alpha = 0°$). According to the TSRS model, we theoretically deduce the formula of the vibration intensity of both the E_g and A_{1g} phonon modes (see Supplementary Note 2). Considering that the doubly degenerate E_g mode owns two second-order Raman tensors of $\boldsymbol{R}(E_g)_1$ and $\boldsymbol{R}(E_g)_2$, the calculated vibration intensity can be expressed as $S_{(Eg)1} \propto |2c^2 \sin(2\alpha)\cos(2\beta)|$ and $S_{(Eg)2} \propto |2c^2 \cos(2\alpha)\sin(2\beta)|$, respectively. For the case of

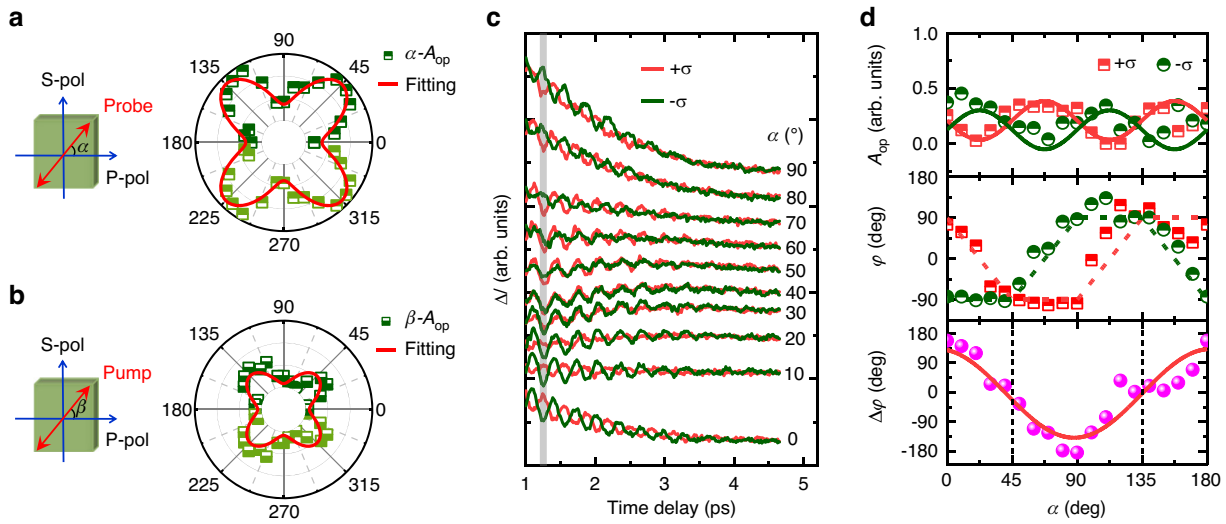

Fig. 3 LP and CP laser-induced anisotropic phonon dynamics. a, **b** The extracted COP amplitudes of E_g mode versus angle α and β for LP excitation, respectively. The angle α (β) is defined as the angle between the linear polarization direction of probe (pump) beam and P-pol direction. The red solid curves represent the best fitted lines via the TSRS model. **c** The time-domain traces at various probe angles for CP excitation. The red (green) lines correspond to the pump excitation with $+\sigma$ ($-\sigma$) helicity light. The curves are vertically shifted for clarity. The vertical grey line indicates the change in phase difference ($\Delta\varphi$) between $+\sigma$ and $-\sigma$ excitation. **d** The fitted A_{op}, φ and $\Delta\varphi$ as a function of α. The solid curves represent the fitted lines according to a sine function

$\beta = 0°$, the $S_{(Eg)2}$ is negligible while $S_{(Eg)1}$ shows a fourfold symmetry with respect to α. This well accounts for the observed experimental results in Fig. 3a. Meanwhile, a β-dependent fourfold symmetry is also extracted from $S_{(Eg)2}$ at $\alpha = 0°$ (Fig. 3b). Therefore, the TSRS model can well explain the observed anisotropy of A_{op}, confirming the ISRS mechanism in the LP excitation of E_g-COP. However, the maximum A_{op} in Fig. 3b is significantly smaller than that in Fig. 3a, indicating that the contributions of two degenerate E_g modes are inequivalent. Moreover, the mode of $\boldsymbol{R}(E_g)_1$ possesses a more remarkable vibration than that of $\boldsymbol{R}(E_g)_2$, which has been demonstrated by the angle-resolved Raman scattering experiments (see Supplementary Notes 3 and 4).

The further investigation is implemented on the anisotropic lattice dynamics following ±σ CP excitation, as shown in Fig. 1e. Figure 3c exhibits a series of transient curve pairs measured with the different probe angle α after pumping with ±σ CP light. By fitting the curves using Eq. (1), the A_{op} and φ values as a function of α are obtained (Fig. 3d). The A_{op} exhibits a fourfold symmetry and has opposite anisotropy for ±σ pumping. Interestingly, the φ value displays a unique variation behavior as a function of α. As α increases from 0° to 45° (or from 90° to 135°), the oscillation phase φ of $+\sigma$ excitation experiences a 180° shift, while that of $-\sigma$ excitation remains almost unchanged. In contrast, when α increases from 45° to 90° (or from 135° to 180°), φ of $-\sigma$ excitation also experiences a 180° shift. The phase difference ($\Delta\varphi$) between the ±σ excitation is also summarized in Fig. 3d, which obeys a relation of $\Delta\varphi = 180°\cdot\sin(2\alpha + 90°)$. It should be noted that similar anisotropy is obtained when the $PtTe_2$ films are rotated by 45°, indicating that the anisotropy is attributed to the optical manipulation rather than $PtTe_2$ crystal orientation.

The physical picture of COP generation via ISRS is schematically shown in Fig. 4a. During the ultrafast femtosecond laser pulse excitation, a photon of frequency f_1 could be converted into another photon of the lower frequency f_2, while releases an E_g mode phonon, satisfying the energy conservation[36]. ISRS can well explain the anisotropic behavior of LP light-driven COP, but cannot account for the exotic α-dependent A_{op} and $\Delta\varphi$ upon CP light excitation through the direct photon-phonon interaction. As discussed above, the COP signals via CP excitation are due to the optical spin injection, i.e., a DECP mechanism that the photoinduced spin-polarized electrons dominate the generation of COP. Here, two possible processes are proposed. First, after the helical light excitation, electrons with the opposite spin orientations at the ground state |g> are excited to a high-energy state with different orbitals (Fig. 4b) according to the spin selection rule[42]. The change of orbital electron distribution disturbs the equilibrium position of the atoms in the crystal, which may have an enhanced or suppressed effect on the E_g-phonons in different vibrational directions. Second, since spin depolarization of the excited electrons experiences within 1 ps, the strong spin-lattice scattering can also

modulate the observed COP vibrational behavior[43,44], where the anisotropic distribution of electron spin may lead to the anisotropic COP behavior.

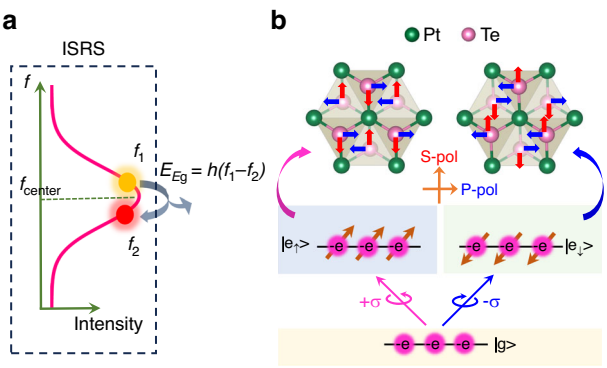

Fig. 4 The physical picture of the anisotropic COP excited by CP light. a The illustration of COP generation by the ISRS mechanism. **b** Excitation of spin-polarized electrons, where |g> is the ground state and $|e_\uparrow>$ (and $|e_\downarrow>$) is the spin-dependent excited state. The middle panel displays E_g-mode oscillations excited by oppositely spin-polarized electrons, in which the red and blue arrows represent the vibrations of Te atoms in the S-pol direction and in the P-pol direction, respectively

Temperature-dependent phonons in $PtTe_2$ films

The temperature-dependent time-domain curves are shown in Fig. 5a to reveal the underlying dissipative mechanism of COP. The difference in transient signals between ΔI $(+\sigma)$ and ΔI $(-\sigma)$ rules out the background signals from hot carriers. It is also compared with the behavior of thermal phonons in frequency-domain spontaneous Raman scattering spectra, as displayed Fig. 5b, where the phonon frequency and the full width at half maximum (FWHM) of Raman shift peak are extracted by Lorentz fitting. By performing theoretical two-temperature model calculations in pump-probe technique and measuring the Stokes and anti-Stokes scattering in Raman spectroscopy, we demonstrate that the increase in local temperature due to laser heating is similar and minimal in both methods (see Supplementary Note 5). Therefore, its impact on the temperature-dependent experiments can be deemed negligible. Figure 5c, d depicts the temperature-dependent frequency of E_g mode by pump-probe technique and Raman spectroscopy, respectively. As temperature increases from 85 to 295 K, both curves exhibit similar linear trends, with a redshift value of ~0.11 (0.10) THz for pump-probe (Raman scattering) spectra. The frequency obtained by pump-probe method is 0.20 THz lower than

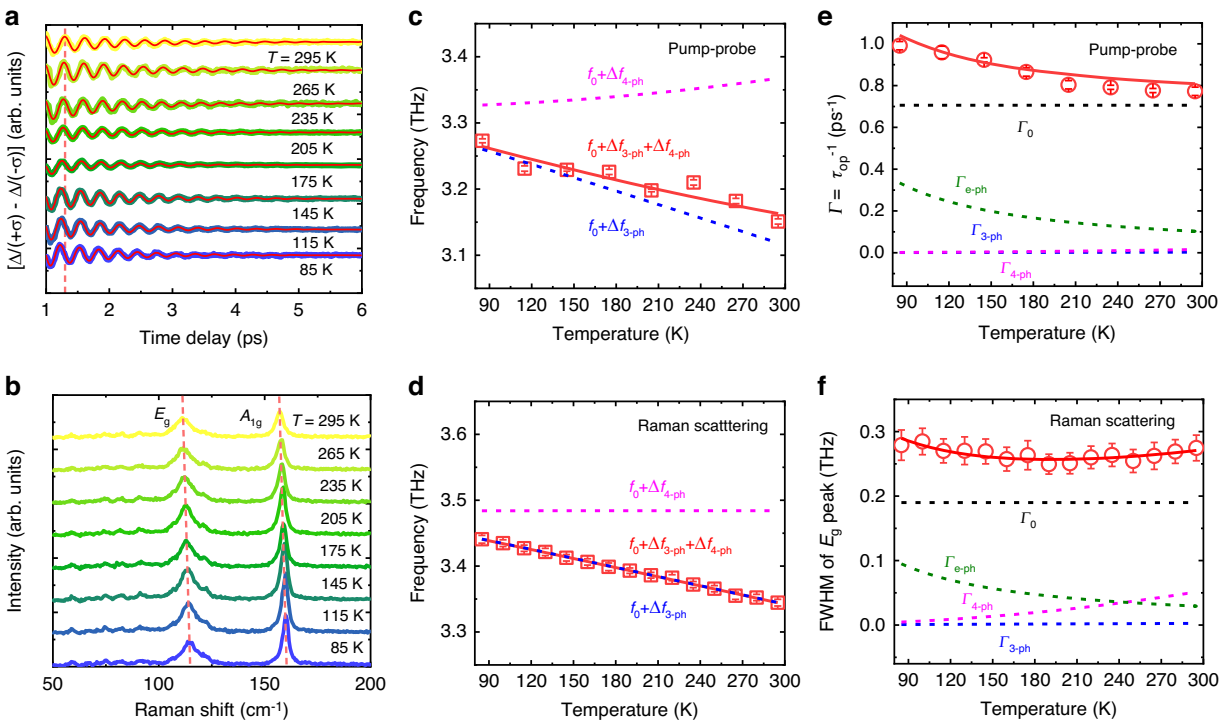

Fig. 5 Temperature-dependent E_g-mode optical phonons. a, **b** The time-domain traces of $[\Delta I(+\sigma) - \Delta I(-\sigma)]$ and the frequency-domain Raman spectra measured at various temperatures, respectively. **c**, **d** The temperature-dependent frequency for E_g-mode phonons derived from (**a**) and (**b**), respectively. **e**, **f** The inverse of COP lifetime (τ_{op}^{-1}) and the FWHM of E_g-mode Raman peak as a function of temperature. The red solid lines are the best fitting using Eqs. (2–4) and Eqs. (5–7), respectively. The blue, purple, and green dashed lines show the corresponding contributions from three-phonon (3-ph), four-phonon (4-ph), and electron-phonon (e-ph) coupling, respectively

that of Raman scattering, which is mainly due to the different mechanisms of the two measurement methods. In the intensive ultrafast pump-probe experiment, the absorption of femtosecond laser energy gives rise to a strong enhancement in electron temperature, leading to electron redistribution at the Fermi energy within several picoseconds. The laser-induced local increase in electron or hole density alters the interatomic interactions, resulting in large internal pressure[45], which reduces the elastic constant and consequently softens the phonon mode. The relationship between phonon softening and photoexcited carrier density is verified by the pump-fluence-dependent experiment shown in Supplementary Note 6.

Usually, the temperature (T)-dependent frequency of optical phonons can be expressed by[46]

$$f(T) = f_0 + \Delta f_{\mathrm{th}}(T) + \Delta f_{\mathrm{ph-ph}}(T) \tag{2}$$

where f_0 accounts for the intrinsic phonon frequency at 0 K, Δf_{th} corresponds to the frequency shift caused by thermal expansion of lattice parameters, and $\Delta f_{\mathrm{ph\text{-}ph}}$ is the frequency shift associated with anharmonic phonon-phonon interaction. The contribution of thermal expansion is described by[47]

$$\Delta f_{\mathrm{th}}(T) = f_0\left\{\exp[-m\gamma\int_0^T a(T')dT'] - 1\right\} \tag{3}$$

where m denotes the degeneracy of the E_{g} mode ($m = 2$), γ is the Grüneisen parameter of the optical Raman mode, and $a(T)$ represents the temperature-dependent linear lattice thermal expansion coefficient. It has been reported that the surface lattice constant of 1T-$PtTe_2$ remains unchanged in the 90–580 K[48], suggesting $a(T)$ is close to zero and the lattice thermal expansion can be negligible. As a result, only the redshift of $\Delta f_{\mathrm{ph\text{-}ph}}$ due to phonon-phonon anharmonicity is taken into account, which can be written as[46]

$$\Delta f_{\mathrm{ph-ph}}(T) = A\left[1 + \frac{2}{e^x - 1}\right] + B\left[1 + \frac{3}{e^y - 1} + \frac{3}{(e^y - 1)^2}\right] \tag{4}$$

The first and second terms represent the three-phonon and four-phonon scattering processes, respectively. A and B are the corresponding fitting parameters. $x = hf_0/2k_{\mathrm{B}}T$ and $y = hf_0/3k_{\mathrm{B}}T$, where h is the Planck constant and k_{B} is the Boltzmann constant. The consistence between the fitting results and the experimental data (Fig. 5c, d) indicates that the anharmonic phonon-phonon interaction is responsible for the energy change of the E_{g} phonons. With the temperature increasing, the four-phonon scattering contribution to frequency ($\Delta f_{\mathrm{4\text{-}ph}}$) either increases (pump-probe method) or keeps almost constant (Raman spectra), indicating that the observed redshift is dominated by three-phonon scattering process.

Figure 5e shows the decay rate ($\Gamma = 1/{\tau_{\mathrm{op}}}^{-1}$) as a function of temperature of the E_{g}-COP derived from Fig. 5a. The gradually decreasing Γ with increasing temperature cannot be simply demonstrated by the anharmonic phonon-phonon scattering model[31]. Another important optical phonon dissipation channel, namely electron-phonon coupling, should be considered, where the decoherence process of phonons is triggered by creating an electron-hole pair[49]. The temperature-dependent decay rate is written as follows[49],

$$\Gamma(T) = \Gamma_0 + \Gamma_{\mathrm{ph-ph}}(T) + \Gamma_{\mathrm{e-ph}}(T) \tag{5}$$

where Γ_0 is the intrinsic decay rate at 0 K, $\Gamma_{\mathrm{ph\text{-}ph}}$ and $\Gamma_{\mathrm{e\text{-}ph}}$ are the decay rate by anharmonic phonon-phonon and electron-phonon scattering, respectively. The $\Gamma_{\mathrm{ph\text{-}ph}}$ term is provided by[46]

$$\Gamma_{\mathrm{ph-ph}}(T) = C\left[1 + \frac{2}{e^x - 1}\right] + D\left[1 + \frac{3}{e^y - 1} + \frac{3}{(e^y - 1)^2}\right] \tag{6}$$

where the fitting parameters C and D represent the three-phonon and four-phonon scattering, respectively. Meanwhile, the temperature-dependent $\Gamma_{\mathrm{e\text{-}ph}}$ can be described as[49]

$$\Gamma_{\mathrm{e-ph}}(T) = \Gamma_{\mathrm{e-ph,0}}\left[\frac{1}{e^{-x} + 1} - \frac{1}{e^x + 1}\right] \tag{7}$$

where $\Gamma_{\mathrm{e\text{-}ph,0}}$ is the residual decay rate from electron-phonon interaction at 0 K. The decay rate $\Gamma_{\mathrm{e\text{-}ph}}$ is proportional to the difference between the number of occupied states of carriers above and below the Fermi level in the energy range of hf_0. According to the Fermi-Dirac distribution, electrons above the Fermi surface and holes below the Fermi surface could inevitably increase with increasing temperature due to the enhanced thermal excitation[49,50]. As a result, the electron-hole pairs excited by optical phonons would be suppressed, giving rise to the observed decreasing tendency of $\Gamma_{\mathrm{e\text{-}ph}}$. The corresponding fitting based on Eqs. (5–7) is shown in Fig. 5e. The different contributions of Γ_0, $\Gamma_{\mathrm{e\text{-}ph}}$, $\Gamma_{\mathrm{3\text{-}ph}}$, and $\Gamma_{\mathrm{4\text{-}ph}}$ are illustrated by dashed lines, in which the value of electron-phonon coupling is much larger than that of phonon-phonon coupling. In addition, only $\Gamma_{\mathrm{e\text{-}ph}}$ drops with increasing temperature, similar to the total decay rate Γ, suggesting that the electron-phonon coupling is dominant. It should be noted that at the higher temperature, the increase rate of $\Gamma_{\mathrm{ph\text{-}ph}}$ will exceed the decrease rate of $\Gamma_{\mathrm{e\text{-}ph}}$, leading to a dominant rising behavior of the total decay rate Γ.

The FWHM of the E_{g} mode in Raman peak, i.e., the thermal phonon decay rate of Γ[46], is shown in Fig. 5f. It is

worth mentioning that the FWHM exhibits a definite nonmonotonic variation behavior as a function of temperature, with a minimum occurring at 210 K. This behavior is very similar to that of the G mode in graphite[51] and E_g mode in $PdTe_2$[52], but completely differs from that of A_{1g} mode, as described in Supplementary Note 7. Obviously, the electron-phonon coupling dominates the decreasing process below 210 K, while the anharmonic phonon-phonon coupling turns to play a primary role above 210 K due to the enhanced contribution of four-phonon scattering.

According to the fitting parameters summarized in Supplementary Table S1 in Supplementary Note 8 and the correlation of $\Gamma_{\text{e-ph},0} = \lambda_{\text{e-ph}} f_0/4$[49,51], the dimensionless electron-phonon coupling strength coefficient $\lambda_{\text{e-ph}}$ can be extracted. The $\lambda_{\text{e-ph}}$ is 0.92 from the pump-probe technique and 0.24 from Raman scattering measurements, respectively, largely consistent with the theoretical calculations (0.35)[53] and the previous experimental observation (0.38–0.42)[48]. These results obtained from time- and frequency-domain measurements suggest a similar dissipation mechanism of the E_g-COP and thermal phonons in $PtTe_2$ films. Furthermore, these results further verify that 1*T*-$PtTe_2$ is a strong electron-phonon coupling material.

Discussion

In conclusion, helicity-dependent excitation of E_g-COP has been observed in Dirac semimetal $PtTe_2$ thin films by using all optical pump-probe spectroscopy, showing the anisotropic oscillation amplitude and phase with respect to the probe light polarization. Unlike the LP light-driven COP that follows the ISRS mechanism, spin-polarized hot electrons dominate the COP vibration excited by $\pm\sigma$ light. In addition, it is revealed that the anharmonic phonon-phonon interaction and electron-phonon scattering determine the temperature-dependent frequency shift and dissipation process of COP, respectively. The electron-phonon coupling strength coefficient of E_g mode is obtained from the time-domain pump-probe and frequency-domain Raman spectroscopy measurements, respectively. This work provides an in-depth understanding of the ultrafast phonon dynamics in topological Dirac semimetals for the potential applications in optoelectronic and opto-spintronic devices.

Materials and methods

The growth of $PtTe_2$ thin films

The 20-nm-thick $PtTe_2$ thin films were grown on the sapphire (Al_2O_3) substrates ($5 \times 5\ mm^2$) by the PLD technique designed for the epitaxial telluride films[54]. The target was prepared by heating the mixed Pt (99.99%) and Te (99.99%) powders with a stoichiometric ratio of 1:2.5 at 450 °C for four days. The basic pressure of the PLD vacuum chamber was maintained at 3×10^{-5} Pa. The $PtTe_2$ films were deposited onto the substrates at 500 °C with a speed of ~1 nm min^{-1} using a 248 nm KrF excimer laser beam (fluence of 1 J cm^{-2} and repetition rate of 2 Hz).

Time-resolved transient measurements

The optical pump-probe technique was used to measure the ultrafast dynamics. A pulsed Ti:sapphire laser (with a central wavelength of 800 nm, a pulse duration of 150 fs, and a repetition rate of 1 kHz) was split into an intensive pump beam (laser fluence of 400 μJ cm^{-2}) under nearly normal incidence and a time-delayed weak probe beam at ~20° incidence with respect to the film normal direction. They were focused onto the same spot with a diameter of 0.8 and 0.2 mm, respectively[55]. Circularly-polarized, elliptically-polarized, and linearly-polarized pump pulses were utilized to excite the dynamic behaviors by rotating a QWP or HWP. The angle $\phi_{\lambda/4}$ of the pump beam is defined as the angle between P-pol and fast axis of a QWP. The incident probe beam was kept LP, with its polarization direction modulated by a HWP. The α (β) is defined as the angle between the LP direction of probe (pump) beam and P-pol direction. The reflected probe pulses entered a balanced photodetector after passing through a HWP and a Wollaston beam splitter. The differential signals ($\Delta I = I_S - I_P$) from the balanced photodetector were acquired with a lock-in amplifier. The setup can simultaneously detect the magneto-optical Kerr effect and anisotropic reflectivity.

Raman scattering experiment

The Raman spectroscopic measurements were carried out on a micro-Raman spectrometer (LabRAM HR 800 UV) with a spectral resolution of 0.5 cm^{-1}, as shown in Fig. S2a. A laser beam with a wavelength of 532 nm and a power of 1.0 mW (25% neutral density filter) was focused onto a spot with a diameter of ~1 μm through a 100× microscope objective (N. A. = 0.9). A multichannel air-cooled CCD (−70 °C) with 1024 × 256 pixels in the spectral range of 200–1050 nm was used to detect Raman scattering signals dispersed on a 1800 grooves/mm grating. Linkam THMSE 600 heating/cooling stage was utilized at a varying temperature rate of 10 K min^{-1} for the temperature-dependent Raman spectra at 85–295 K. In order to further check the anisotropy of the excited phonons in $PtTe_2$, angle-resolved polarized Raman spectra were recorded in a backscattering geometry under the θH and θV scattering configuration. As shown in Fig. S2b and S2c, the film surface was lying the *x*-*y* plane and the incident laser was along the *z*-axis. θ is the angle between the direction of the incident LP light and the *y*-axis. The θH configuration corresponded to the analyzer along the *x*-axis, while the θV configuration was set with

the analyzer parallel to the y-axis[56]. During the measurement, the sample was kept stationary and the polarization angle θ of the incident LP light was changed by rotating a HWP, which rotated at 10° in every step.

Acknowledgements
The authors are grateful to Bowen Li and Prof. Qi Zhang for the additional Raman measurements. This work was supported by the National Key R&D Program of China (2022YFA1402404), the National Natural Science Foundation of China (12374104, 52171230, T2394473, T2394470, 62274085, 61822403 and 11874120) and the Fundamental Research Funds for the Central Universities (021014380225).

Author details
[1]Key Laboratory of Micro and Nano Photonic Structures (MOE), School of Information Science and Technology, Fudan University, Shanghai, China. [2]Jiangsu Provincial Key Laboratory of Advanced Photonic and Electronic Materials, State Key Laboratory of Spintronics Devices and Technologies, School of Electronic Science and Engineering, Collaborative Innovation Center of Advanced Microstructures, Nanjing University, Nanjing, China. [3]Department of Physics, School of Physics and Electronic Science, East China Normal University, Shanghai, China. [4]Department of Physics, Xiamen University, Xiamen, China

Author contributions
Z.Z. and X.W. conceived and designed the study. R.Z. supervised the project. Z.L. and Y.C. performed the experiments and analyzed the data. A.S. contributed to the sample growth. J.Z. performed the Raman scattering measurements. All the authors discussed the results. Z.L., Y.C., Z.Z. and X.W. wrote the manuscript with contributions from all the authors.

Data availability
The data that support the plots in this paper and other findings of this study are available from the corresponding authors upon reasonable request.

Conflict of interest
The authors declare no competing interests.

Supplementary information The online version contains supplementary material available at https://doi.org/10.1038/s41377-024-01540-z.

Received: 2 March 2024 Revised: 4 July 2024 Accepted: 17 July 2024
Published online: 01 August 2024

References

1. Liu, Z. K. et al. Discovery of a three-dimensional topological Dirac semimetal, Na_3Bi. *Science* **343**, 864–867 (2014).
2. Neupane, M. et al. Observation of a three-dimensional topological Dirac semimetal phase in high-mobility Cd_3As_2. *Nat. Commun.* **5**, 3786 (2014).
3. Hu, M. Y. et al. Double-bowl state in photonic Dirac nodal line semimetal. *Light Sci. Appl.* **10**, 170 (2021).
4. Rizza, C. & Molle, A. Closing the THz gap with Dirac semimetals. *Light Sci. Appl.* **11**, 124 (2022).
5. Armitage, N. P., Mele, E. J. & Vishwanath, A. Weyl and Dirac semimetals in three-dimensional solids. *Rev. Mod. Phys.* **90**, 015001 (2018).
6. Bansil, A., Lin, H. & Das, T. *Colloquium*: topological band theory. *Rev. Mod. Phys.* **88**, 021004 (2016).
7. Yan, M. Z. et al. Lorentz-violating type-II Dirac fermions in transition metal dichalcogenide $PtTe_2$. *Nat. Commun.* **8**, 257 (2017).
8. Amit, S. R. K. et al. Type-II Dirac semimetal candidates ATe_2 (A=Pt, Pd): a de Haas-van Alphen study. *Phys. Rev. Mater.* **2**, 114202 (2018).
9. Fu, D. Z. et al. Quantum oscillations in type-II Dirac semimetal $PtTe_2$. *Phys. Rev. B* **97**, 245109 (2018).
10. Xu, H. J. et al. High spin hall conductivity in large-area type-II Dirac semimetal $PtTe_2$. *Adv. Mater.* **32**, 2000513 (2020).
11. Fu, L. et al. Highly organized epitaxy of Dirac semimetallic $PtTe_2$ crystals with extrahigh conductivity and visible surface plasmons at edges. *ACS Nano* **12**, 9405–9411 (2018).
12. Ma, H. F. et al. Thickness-tunable synthesis of ultrathin type-II Dirac semimetal $PtTe_2$ single crystals and their thickness-dependent electronic properties. *Nano Lett.* **18**, 3523–3529 (2018).
13. Song, S. et al. Air-stable van der Waals $PtTe_2$ conductors with high current-carrying capacity and strong spin-orbit interaction. *iScience* **25**, 105346 (2022).
14. Lin, M. K. et al. Dimensionality-mediated semimetal-semiconductor transition in ultrathin $PtTe_2$ films. *Phys. Rev. Lett.* **124**, 036402 (2020).
15. Zeng, L. H. et al. Van der Waals epitaxial growth of mosaic-like 2D platinum ditelluride layers for room-temperature mid-infrared photodetection up to 10.6 μm. *Adv. Mater.* **32**, 2004412 (2020).
16. Deng, K. et al. Crossover from 2D metal to 3D Dirac semimetal in metallic $PtTe_2$ films with local Rashba effect. *Sci. Bull.* **64**, 1044–1048 (2019).
17. Wei, T. Y. et al. Mid-infrared photodetection of type-II Dirac semimetal 1T-$PtTe_2$ grown by molecular beam epitaxy. *ACS Appl. Mater. Interfaces* **13**, 22757–22764 (2021).
18. Tong, X. W. et al. Direct tellurization of Pt to synthesize 2D $PtTe_2$ for high-performance broadband photodetectors and NIR image sensors. *ACS Appl. Mater. Interfaces* **12**, 53921–53931 (2020).
19. Xu, H. et al. $PtTe_2$-based type-II Dirac semimetal and its van der Waals heterostructure for sensitive room temperature terahertz photodetection. *Small* **15**, 1903362 (2019).
20. Shawkat, M. S. et al. Scalable van der Waals two-dimensional $PtTe_2$ layers integrated onto silicon for efficient near-to-mid infrared photodetection. *ACS Appl. Mater. Interfaces* **13**, 15542–15550 (2021).
21. Chen, Z. Q. et al. Defect-induced helicity dependent terahertz emission in Dirac semimetal $PtTe_2$ thin films. *Nat. Commun.* **15**, 2605 (2024).
22. Wang, M. C. et al. Unraveling photoinduced spin dynamics in the topological insulator Bi_2Se_3. *Phys. Rev. Lett.* **116**, 036601 (2016).
23. Dai, Y. M. et al. Ultrafast carrier dynamics in the large-magnetoresistance material WTe_2. *Phys. Rev. B* **92**, 161104 (2015).
24. Afanasiev, D. et al. Ultrafast control of magnetic interactions via light-driven phonons. *Nat. Mater.* **20**, 607–611 (2021).
25. Rini, M. et al. Control of the electronic phase of a manganite by mode-selective vibrational excitation. *Nature* **449**, 72–74 (2007).
26. Mankowsky, R. et al. Nonlinear lattice dynamics as a basis for enhanced superconductivity in $YBa_2Cu_3O_{6.5}$. *Nature* **516**, 71–73 (2014).
27. Alfano, R. R. & Shapiro, S. L. Optical phonon lifetime measured directly with picosecond pulses. *Phys. Rev. Lett.* **26**, 1247–1251 (1971).
28. Alfano, R. R. & Shapiro, S. L. Establishment of a molecular-vibration decay route in a liquid. *Phys. Rev. Lett.* **29**, 1655–1658 (1972).
29. Laubereau, A. & Kaiser, W. Vibrational dynamics of liquids and solids investigated by picosecond light pulses. *Rev. Mod. Phys.* **50**, 607–665 (1978).
30. Tsen, K. T. et al. Electron-optical-phonon interactions in ultrathin GaAs/AlAs multiple quantum wells. *Phys. Rev. Lett.* **67**, 2557–2560 (1991).
31. Cheng, L. et al. Ultrafast carrier and lattice dynamics in the Dirac semimetal $NiTe_2$. *Phys. Rev. B* **106**, 104308 (2022).
32. Suo, P. et al. Ultrafast photocarrier and coherent phonon dynamics in type-II Dirac semimetal $PtTe_2$ thin films probed by optical spectroscopy. *Photonics Res.* **10**, 653–661 (2022).
33. Glamazda, A. et al. Proximity to a commensurate charge modulation in $IrTe_{2-x}Se_x$ ($x = 0$ and 0.45) revealed by Raman spectroscopy. *N. J. Phys.* **16**, 093061 (2014).
34. Hsieh, D. et al. Selective probing of photoinduced charge and spin dynamics in the bulk and surface of a topological insulator. *Phys. Rev. Lett.* **107**, 077401 (2011).
35. Li, N., Liang, W. Z. & Luo, S. N. Hot carrier dynamics and phonon anharmonicity of $ZrTe_5$ revealed with femtosecond transient optical spectroscopy. *Phys. Rev. B* **101**, 014304 (2020).
36. Dhar, L., Rogers, J. A. & Nelson, K. A. Time-resolved vibrational spectroscopy in the impulsive limit. *Chem. Rev.* **94**, 157–193 (1994).
37. Zeiger, H. J. et al. Theory for displacive excitation of coherent phonons. *Phys. Rev. B* **45**, 768–778 (1992).
38. Jeong, T. Y. et al. Coherent lattice vibrations in mono- and few-layer WSe_2. *ACS Nano* **10**, 5560–5566 (2016).
39. Zhu, S. X. et al. Temperature evolution of quasiparticle dispersion and dynamics in semimetallic 1T—$TiTe_2$ via high-resolution angle-resolved photoemission spectroscopy and ultrafast optical pump-probe spectroscopy. *Phys. Rev. B* **103**, 115108 (2021).

40. Garrett, G. A. et al. Coherent THz phonons driven by light pulses and the Sb problem: what is the mechanism? *Phys. Rev. Lett.* **77**, 3661–3664 (1996).
41. Shalini, A. et al. Observation of T_2-like coherent optical phonons in epitaxial $Ge_2Sb_2Te_5$/GaSb(001) films. *Sci. Rep.* **3**, 2965 (2013).
42. Reid, A. H. M. et al. Investigation of the femtosecond inverse Faraday effect using paramagnetic $Dy_3Al_5O_{12}$. *Phys. Rev. B* **81**, 104404 (2010).
43. Khusyainov, D. et al. Ultrafast laser-induced spin–lattice dynamics in the van der Waals antiferromagnet $CoPS_3$. *APL Mater.* **11**, 071104 (2023).
44. Padmanabhan, P. et al. Coherent helicity-dependent spin-phonon oscillations in the ferromagnetic van der Waals crystal CrI_3. *Nat. Commun.* **13**, 4473 (2022).
45. Yan, G. Q. et al. Different effects of electronic excitation on metals and semiconductors. *Phys. Rev. B* **93**, 214302 (2016).
46. Tang, H. & Herman, I. P. Raman microprobe scattering of solid silicon and germanium at the melting temperature. *Phys. Rev. B* **43**, 2299–2304 (1991).
47. Postmus, C., Ferraro, J. R. & Mitra, S. S. Pressure dependence of infrared eigenfrequencies of KCl and KBr. *Phys. Rev.* **174**, 983–987 (1968).
48. Anemone, G. et al. Experimental determination of surface thermal expansion and electron–phonon coupling constant of 1T-$PtTe_2$. *2D Mater.* **7**, 025007 (2020).
49. Bonini, N. et al. Phonon anharmonicities in graphite and graphene. *Phys. Rev. Lett.* **99**, 176802 (2007).
50. Xu, B. et al. Temperature-tunable Fano resonance induced by strong coupling between Weyl fermions and phonons in TaAs. *Nat. Commun.* **8**, 14933 (2017).
51. Liu, H. N. et al. The intrinsic temperature-dependent Raman spectra of graphite in the temperature range from 4K to 1000K. *Carbon* **152**, 451–458 (2019).
52. Al-Makeen, M. M. et al. Investigation of the electron–phonon coupling in Dirac semimetal $PdTe_2$ via temperature-dependent Raman spectroscopy. *Phys. Status Solidi (RRL) - Rapid Res. Lett.* **16**, 2200257 (2022).
53. Kim, K. et al. Importance of the van Hove singularity in superconducting $PdTe_2$. *Phys. Rev. B* **97**, 165102 (2018).
54. Chen, Y. Q. et al. Observation of colossal topological hall effect in noncoplanar ferromagnet Cr_5Te_6 thin films. *Adv. Funct. Mater.* **33**, 2302984 (2023).
55. Wu, G. J. et al. Tuning magnetization dynamics with strong spin-orbit coupling in transition-metal dichalcogenide/Co-Fe-B heterostructures. *Phys. Rev. Appl.* **13**, 024027 (2020).
56. Liu, X. L. et al. Different angle-resolved polarization configurations of Raman spectroscopy: a case on the basal and edge plane of two-dimensional materials. *Chin. Phys. B* **26**, 067802 (2017).